

# Divergent Design of Mechanical Metamaterials Clan Deducted from Arc-serpentine Curve

Shengli Mi (✉ [mi.shengli@sz.tsinghua.edu.cn](mailto:mi.shengli@sz.tsinghua.edu.cn))

Tsinghua University

Hongyi Yao

Tsinghua University

Xiaoyu Zhao

Tsinghua University

Wei Sun

Tsinghua University

---

## Article

### Keywords:

**Posted Date:** December 15th, 2021

**DOI:** <https://doi.org/10.21203/rs.3.rs-753485/v1>

**License:** © ⓘ This work is licensed under a Creative Commons Attribution 4.0 International License.

[Read Full License](#)

---

# Divergent Design of Mechanical Metamaterials Clan Deducted from Arc-serpentine Curve

## Abstract

The exotic properties of mechanical metamaterials are determined by their unit-cells' structure and spatial arrangement, in analogy with the atoms of conventional materials. Companioned with the mechanism of structural or cellular materials<sup>1-5</sup>, the ancient wisdom of origami<sup>6-11</sup> and kirigami<sup>12-16</sup> and the involvement of multiphysics interaction<sup>2,17,18</sup> enrich the programable mechanical behaviors of metamaterials, including shape-morphing<sup>8,12,14,16,19</sup>, compliance<sup>4,5,8,17,20</sup>, texture<sup>2,18,21</sup>, and topology<sup>11,18,22-25</sup>. However, typical design strategies are mainly convergent, which transfers various structures into one family of metamaterials that are relatively incompatible with the others and do not fully bring combinatorial principles<sup>3,10,26</sup> into play. Here, we report a divergent strategy that designs a clan of mechanical metamaterials with diverse properties derived from a symmetric curve consisting of serpentine and arcs. We derived this composite curve into planar and cubic unit-cells and modularized them by attaching magnetics. Moreover, stacking each of them yields two- and three-dimensional auxetic metamaterials, respectively. Assembling with both modules, we achieved three thick plate-like metamaterials separately with flexibility, in-plane buckling, and foldability. Furthermore, we demonstrated that the hybrid of paradox properties is possible by combining two of the above assembles. We anticipate that this divergent strategy paves the path of building a hierarchical library of diverse combinable mechanical metamaterials and making conventional convergent strategies more efficient to various requests.

# Main

## *Introduction*

Many outstanding efforts of creating a family of mechanical metamaterials with one specific meta-property or functionality have been achieved convergently by intuitive guidance and rational induction. Conversely, we report a divergent process focusing on the diversity and universality between a couple of metamaterials' families deduced from one type of geometry. The design philosophy of Lego parts provides an ideal reference to help us figure out the essential elements and workflow of our divergent strategy.

The bricks of the Lego Technic series possess at least one hole, which is the basic unit of measuring the sizes of any Lego object, serving as a universal interface to interlock with other bricks. Moreover, the structural bricks, such as liftarms, frames, and plates, can be divided into two categories, one with one stacking direction and the other with multiple stacking directions. These two features facilitate players to build complex Lego objects via stacking various structural bricks with the assistance of auxiliary bricks (including pins, nuts, and axles). Inspired by the facts above, we concluded three essential elements to construct a divergent design procedure, thus, (i) A fundamental part containing one universal interface, which is the gene of the unit-cells of the followed metamaterials, (ii) a deductive procedure that patterns the fundamental part into mono-stackable and pluri-stackable parts, and (iii) a stacking mechanism companioned with auxiliary features (or fasteners), which assembles above parts into complex modulus and hybrid metamaterials (as shown in Figure 1a).

Besides, a myriad of Lego MOCs (My Own Creation, the assemblies designed by players rather than authority), ranging from static artworks of centimeter-scale to dynamic vehicles of meter-scale, can be assembled by finite types of bricks sharing a universal and reversible interlocking mechanism. This mechanism works like the genes or spirits of a clan, which unites the members from various families, even across generations, together to create new content under the changing times and circumstances. Inspired by this fact, we introduce a concept of the mechanical metamaterials clan whose members' unit-cells are diverse while derived from the exact origin. The divergent deduction endows diversities to these cells. Simultaneously, the same ancestor maintains their universal interfaces to combine them as hybrid ones that exhibit targeted or unexpected responses. In the following, we depict our divergent design by introducing the fundamental part and deducing it into six families of mechanical metamaterials.

### *Fundamental part and deductive procedure*

Inspired by the pattern of the Taichi, which is symbolized as the ultimate origin of the Universe in Chinese ancient philosophy, we proposed the arc-serpentine element (ASC), which comprises a serpentine<sup>27,28</sup> extended by tangentially attached circular arcs, as the blueprint of the fundamental part. Two semicircles with opposite signs of curvatures construct the serpentine(as shown in Figure1c). Hence, an individual ASC is not superimposable on its mirror image and can be left-handed or right-handed. We define that an ASC whose curvature transits from positive to negative is left-handed and vice versa (as shown in Figure1e). Then, we transfer a left-handed ASC into a planar, curved beam whose cross-section is rectangular and referred to as a point object, denoted as  $X^{(0)}$  and  $\overline{X^{(0)}}$  for right-handed one(Figure1c). We set the thickness as double times larger than the width, which constraints the out-plane deformation. We investigated the distribution of elastic energy density along the neutral curve of  $X^{(0)}$  under rotation, shear, and uniaxial compression and stretch by simulation. The result shows the deformation of  $X^{(0)}$  remains in-plane. Moreover, the deformation mainly occurs in the arc segment, and the central area of the serpentine segment has lower deformation energy, which means the elastic deformation of this part is negligible, and only rigid rotation and translation exist. Consequently, we choose the midpoint of this  $X^{(0)}$  (also the center of its serpentine) as the anchor of the universal interface, refer to as stack point, which will be fulfilled as a cylindric pin embedded or attached on the anchor in the following procedure.

Next, we introduce a "point-line-face" strategy that transfers  $X^{(0)}$  into its two derivative objects, i.e., line object (denoted as  $X^{(1)}$ ) and face object (denoted as  $X^{(2)}$ ). We connect  $n$   $X^{(0)}$ s with interlaced handedness by merging specific connect vertices, overlapping the corresponding end faces, and achieving a line object  $X^{(1)}(X^{(0)}, n)$ , as shown in path-1 in Figure1d. Moreover, the  $X_{nO}^{(1)}$  is an open line object comprising  $n$   $X^{(0)}$  s, while the  $X_{mC}^{(1)}$  is a closed line object comprising  $m$   $X^{(0)}$  s (whose parameters are varied from the ones of  $X^{(0)}$ ), which can also be treated as a polygon. For each  $X^{(0)}$  of  $X_{mC}^{(1)}$ , we change the central angle corresponding to the arc segment to achieve the change of angle between their head and tail velocity vectors. We investigated the mechanical behaviors of  $X_{6O}^{(1)}$  under the uniaxial compression by simulation(Extended Data Figure1). Although the length of  $X_{6O}^{(1)}$  is six times larger than the one of  $X^{(0)}$ , which is prone to exhibit out-plane bulking for a ribbon with the same size, the deformation of  $X_{6O}^{(1)}$  still occurs in-plane. This is because the arc segment of  $X_{6O}^{(1)}$

provides the degree of freedom (DoFs) to bend in-plane, making it more susceptible to lateral buckling when subjected to compressive loads.

Based on these facts, we propose a stacking operation that overlaps the centers of two ASCs and stacks them as a double-layer structure. So, by stacking several  $X_{nO}^{(1)}$  on  $X_{mC}^{(1)}$  via their specific stack point and linking them by a cylinder whose central axis goes through their centers, we achieved a face unit  $X^{(2)}$  with a predesigned layout. The topology of the layout is arbitrary, and the layout elements need to meet the condition that there are only one polygon and no less than three open curves connected to it. These polygons and curves are fulfilled as  $X_{nO}^{(1)}$  and  $X_{mC}^{(1)}$ . The chirality coupling linear deformation and rotation plays a significant role in the design of mechanical metamaterials<sup>3,4,15,29-31</sup>. Without loss of generality, the layout adopted in this article is a tetrarchical unit<sup>30</sup>, stacking four  $X_{3O}^{(1)}$  and one  $X_{8C}^{(1)}$  as a  $X^{(2)}(X_{3O}^{(1)}, 4, X_{8C}^{(1)}, 1)$  (Hereafter abbreviated as  $\widehat{X}^{(2)}$ ) as shown in path-2 in Figure1d. The responsive definition of the handedness of  $X^{(2)}$  is discussed in supporting materials.

It is worth noting that the nature of in-plane bulking undergoing compression of  $X^{(1)}$ s makes them not interfere with each other when they are deformed in coordination as one  $X^{(2)}$ . Since  $\widehat{X}^{(2)}$  has four  $X_{3O}^{(1)}$  uniformly distributed around one  $X_{8C}^{(1)}$ , it can undergo the loads along the X- and Y-axis simultaneously. Therefore, as shown in Extended Data Figure3, we simulate the deformation behavior of  $X^{(2)}$  under two types of load application (X- or Y-axis loading alone or both X- and Y-axis loading). We observed that the  $X_{8C}^{(1)}$  of  $\widehat{X}^{(2)}$  undergoes both shear and rotation under uniaxial loading. In contrast, it maintains its initial shape with only rigid rotation under biaxial loading, which is due to the fact that the resultant force of the biaxial loads is zero and the resultant moment is non-zero. This recurrence of chirality allows us to utilize the topology of chiral auxetic metamaterials to expand  $\widehat{X}^{(2)}$  into mono-stackable modulus whose size is  $n \times m$ , denoted as  $\widehat{X}_{n \times m}^{(2)}$ .

Finally, we combine several  $X^{(2)}$

$X^{(3)}(X^{(2)}, \Xi)$ , where  $\Xi$

$\widehat{X}^{(2)}$ , a square, the corresponding shape of  $\widehat{X}^{(3)}$

$$\Xi_1 = ABCDEF$$

for left-handedness and  $\Xi_2 = \overline{ABCDEF}$

$\widehat{X}^{(2)}$  s in one  $\widehat{X}^{(3)}$  . One is an  $\widehat{X}^{(2)}$  connecting four  $\widehat{X}^{(2)}$  s (denoted as  $\widehat{X}^{(2)}|_{c=4}$  , where  $c$  is the number of the connected adjacent facets), and the other is an  $\widehat{X}^{(2)}$  centrosymmetrically connecting two  $\widehat{X}^{(2)}$  s (denoted as  $\widehat{X}^{(2)}|_{c=2}$  ). Correspondingly, there are two kinds of primary loading conditions for  $\widehat{X}^{(3)}$  . We simulate and analyze the mechanical behavior of the load (including compression/stretching, shear, bending, and twist) acting on the pair of  $\widehat{X}^{(3)}|_{c=4}$  faces and pair of  $\widehat{X}^{(3)}|_{c=2}$  faces, respectively. The deformed shape of  $\widehat{X}^{(3)}$  is characterized by the ratio  $\alpha$  of the magnitude of principal strain  $\|\varepsilon\|$  and volumetric strain  $\delta$  . We observed that volumetric expansion (or shrinking) of  $\widehat{X}^{(3)}$  ( $\alpha=0.577$ ) is triggered by twist, and the Poisson's ratio of  $\widehat{X}^{(3)}$  maintains zero during compression/stretching (we fix the Dof of rotation of acted facets) in both situations. However, as shown in the Extended Data Figure4-5, the normalized effective stiffness  $\bar{K}$  is larger when  $\widehat{X}^{(3)}|_{c=4}$  is acted by shear and bending load along given direction than the one of  $\widehat{X}^{(3)}|_{c=2}$  , (the ratio between the former and latter are 1.5~1.71 for shearing and 1.48~3.79 for bending), which is due to the geometric frustration of  $\widehat{X}^{(3)}$  brought by its rigid corner and facets(Extended Data Figure4-5). It is worth noting that all the six  $X_{8C}^{(1)}$  s of  $\widehat{X}^{(3)}$  are prone to maintain planar during the above circumstances, which makes a  $\widehat{X}^{(3)}$  as a pluri-stackable modulus with three stacking directions.

### *Variant design*

The twist-triggered volumetric deformation of  $\widehat{X}^{(3)}$   $X_{8C}^{(1)}$

$X_{3O}^{(1)}$

$\widehat{X}^{(2)}$  and  $\widehat{X}^{(3)}$  which adjusts their sizes and expands the space of desired expansion (or compression). To start with, we fixed the shape of  $X_{8C}^{(1)}$  s. This idealization gives us a shortcut of evaluating the targeted deformation of  $\widehat{X}^{(2)}$  by rotating its  $X_{8C}^{(1)}$

$X_{3O}^{(1)}$

$\theta_{ij}^k (i = 1, 4, j = 1, 2, 3, k = 1, 2, \dots, 4)$ , which is the central angle of the  $i$

$j^{\text{th}}$  arc of the  $X^{(0)}$  of the  $k^{\text{th}}$   $X_{30}^{(1)}$  in a  $\widehat{X}^{(2)}$ . Finally, following the principle of minimum elastic energy, we get the optimized value  $\tilde{\theta}_{ij}^k = \theta_{ij}^k + \delta\theta_{ij}^k$ , where  $\delta\theta_{ij}^k$  are solved by solving

$$\min_{\delta\theta_{1j}^k, \delta\theta_{4j}^k} \sum_{k=1}^4 \sum_{j=1}^3 ((\delta\theta_{1j}^k)^2 + (\delta\theta_{4j}^k)^2) \quad (1)$$

while satisfying the constraints imposed by given displacement boundary conditions. With this variant design, we can expand each of the following assembled metamaterials into a family whose member's unit-cells are the variants of the original one.

### *Assembling mechanical metamaterials by stacking*

Since modules can assemble a mechanical metamaterial following a given topology, the characters of the module determine the properties of resulted metamaterials that possess the same topology. For convenience, the default topology of the metamaterials investigated here is equivalent to the ones of continuous material. Since the mechanical metamaterials assembled by one type of cells are the cornerstones of the whole family, we refer to them as fundamental mechanical metamaterials (FMMs). We glued cylindrical magnets with suitable magnetic poles to all the stacking points on  $\widehat{X}_{n \times m}^{(2)}$  (Extended Data Figure2b), making it a mono-stackable module, denoted as  $M^{(1)}(\widehat{X}_{n \times m}^{(2)})$  that can be assembled through magnetic adsorption. Similarly, we transfer  $\widehat{X}^{(3)}$  as a pluri-stackable module with three orthogonal stacking directions, denoted as  $M^{(3)}(\widehat{X}^{(3)})$ . We stacked  $M^{(1)}(\widehat{X}_{2 \times 2}^{(2)})$ s into a double layer sheet(Figure2a), denoted as FMM-I, which exhibits a negative Poisson's ratio of -0.81(Figure2c).

Similarly, we assembled  $M^{(3)}(\widehat{X}^{(3)})$ s along three dimensions and gained a bulk auxetic material(Figure2d), denoted as FMM-II, whose Poisson's ratio is -0.76, as shown in Figure2g. The initial geometry of  $M^{(3)}(\widehat{X}^{(3)})$  is capable of varied by the method we mentioned before(Figure2e). These assemblies show similar properties with their modular(Extended Data Figure3-5). The results show that the mechanical properties of FMM are consistent with the ones of its module (unit-cell).

Furthermore, two moduli are capable of combining as a new one. The responsive assemblies are referred to as derived mechanical metamaterial (DMM) since their building cells are derived from fundamental ones. The modulus of these materials is referred to as derived modulus. We derived three kinds of derived modulus as shown in path-4 in Figure1d and Figure3a-c. To begin with, we stacked

$M^{(1)}(\widehat{X}_{1 \times 2}^{(2)})$ s on the lateral faces of  $M^{(3)}(\widehat{X}^{(3)})$  and assembled these hybrid tetrarchical units (denoted as  $M^{(3)}(\widehat{X}^{(3)} + 4\widehat{X}_{1 \times 2}^{(2)})$ ) as a flexible thick plate. This plate, denoted as DMM-I, is compliant to vary its Gaussian curvature from negative to positive due to intrinsic deformation properties of  $M^{(3)}(\widehat{X}^{(3)})$  and extra degree of freedom (DoF) of bending and torsion brought by  $M^{(1)}(\widehat{X}_{1 \times 2}^{(2)})$ , as shown in Figure3d. This combination fulfills the DoF of each  $M^{(3)}(\widehat{X}^{(3)})$  to six and makes their positions and orientations adaptive to arbitrary situations.

Next, we assembled a sandwich compound structure (denoted as  $M^{(3)}(5\widehat{X}^{(3)} + 2\widehat{X}_{3 \times 3}^{(2)})$ ) whose wall layers are  $M^{(1)}(\widehat{X}_{3 \times 3}^{(2)})$  and connected by five  $M^{(3)}(\widehat{X}^{(3)})$ s at the corner and center of tessellation. The metamaterials consisted of these moduli, denoted as DMM-II, which occurs in-plane bulking under compression(Figure3e). This unexpected non-linear behavior is dominated by the shear deformations of its modulus, resulting from geometric frustration, which is because that the directions of inner stacking and outer combinations are orthogonal, transferring part of the compression load of the boundaries to the torque acting on each  $M^{(3)}(\widehat{X}^{(3)})$  along the axis perpendicular to the deformation plane.

Finally, we added three  $M^{(3)}(\widehat{X}^{(3)})$ s between each pair of  $M^{(3)}(5\widehat{X}^{(3)} + 2\widehat{X}_{3 \times 3}^{(2)})$ s and achieved an auxetic and foldable thick plate, denoted as DMM-III. Every three  $M^{(3)}(\widehat{X}^{(3)})$ s connect as a pillar which works as a blend of linear spring and plane joint, decreasing the total DoF of the connected four  $M^{(3)}(\widehat{X}^{(3)})$ s from 16 to 4. This fact guarantees the whole metamaterials get rid of geometric frustration and serves as a Muri-ori modular which can be folded into the shapes with all ranges of Gaussian curvature (Figure3f) and acts as a fundamental element of large-scale origami metamaterials.

To explore the combinatorial functions between different clan members, we combined FMM-II and DMM-I and resulted in a hybrid mechanical metamaterial (HMM), denoted as HMM-I(Figure4). Although the stack points of the above two materials are geometrically incompatible in their natural state, as shown in Figure4, they are still capable of stacking as a hybrid one owing to compatible deformation. In hybrid state, FMM-II constraints  $M^{(3)}(\widehat{X}^{(3)})$ s of DMM-I to adapt its tessellation resulted in the rotations of the lateral components of each  $M^{(3)}(\widehat{X}^{(3)})$ s. As we have demonstrated

above, FMM-II is auxetic, and DMM-I is thick while compliant to a non-planar surface. However, their strengths happen to be properties that the other party cannot possess. FMM-II could not maintain its flexibility if the thickness increased to the same size as the one's of DMM-I and DMM-I does not exhibit auxetic deformation under the same boundary conditions of FMM-II. Consequently, it is worth noting that HMM-I equips these two properties at the same time. The experiments show that the Poisson's ratio is  $-0.75$ , and HMM-1 is flexible to adapt to the non-planar surface with positive Gaussian curvature(Figure4d).

### *Conclusion*

In summary, we have demonstrated that how ASCs can be exploited by a divergent design strategy to build a clan of mechanical metamaterials. Although the unit-cells of these metamaterials(summarized in Extended Data table1) all can be categorized as slender, they also show the behaviors that are more pervasive in the metamaterials created by the mechanism of origami and kirigami. Moreover, the change of geometric parameters and topology of the point, face, and volume object are the three independent ways that create more collateral branches of this clan. Hence, the diversity and connectivity among the plentiful members of this clan reveal ample space to discover exotic properties via combinatorial methods. Furthermore, the algorithm applied for physical engines, such as position-based dynamics<sup>32-35</sup>, combined with finite element analysis and can provide efficient numerical tools to guide such exploration. Finally, assisted by our divergent strategy, the request-based convergent design and fabrication of the multiscale mechanical metamaterials can be more compliant, economical, and adaptive for various scenarios, including bioprinting, soft robotics, and wearable device.

## Methods

### *Theoretical model*

The details of the mathematic model of our divergent strategy are summarized in Supplementary Information sections 1-5. The variation method of face and volume object is described in Supplementary Information sections 6.

### *Fabrication of modules and metamaterials*

We implemented the mathematic model derived above in MATLAB(Mathworks, U.S.) and generate geometries of face objects  $\widehat{X}^{(2)}$ , including the original  $\widehat{X}_{1 \times 1}^{(2)}$  and expanded objects ( $\widehat{X}_{1 \times 3}^{(2)}, \widehat{X}_{1 \times 2}^{(2)}, \widehat{X}_{2 \times 2}^{(2)}, \widehat{X}_{3 \times 3}^{(2)}$ ) and volume objects  $\widehat{X}^{(3)}$ . These geometries were exported as STL files and fabricated with a volumetric scale of 0.2 by MultiJet(MJP) 3D printing (ProJet 3510 HD, 3D Systems) and colored by spray painting. The cylindrical magnetics were attached on the stack points of  $F^*$  and  $V^*$  by U.V. light-curing adhesive.

### *Simulation*

We recreate the above geometries in COMSOL Multiphysics(COMSOL, U.S.) with the geometric parts method. Then, fully meshed finite element analysis (FEA) simulations were used to check the mechanical response of point object  $X^{(0)}$ , line object  $X_{60}^{(1)}$ , face object  $\widehat{X}_{1 \times 1}^{(2)}$ , and volume object  $\widehat{X}^{(3)}$ , all with left-handedness. The Young's modulus of the materials adopted in these analyses is 127Mpa, which is the same as the one utilized in fabrication. We fixed one end face of  $X^{(0)}$  and applied a displacement condition with a magnitude of 30mm. For  $X_{60}^{(1)}$ , we maintain the fixed condition and increase the magnitude of the displacement condition to 180mm. Moreover, we also replace this displacement condition with a rotation condition whose magnitude is 45 degrees. There are two kinds of configurations of the displacement whose magnitude is 30mm applied on  $\widehat{X}_{1 \times 1}^{(2)}$ . One is all four end faces applied and the other is two symmetric ones of them. The magnitude of the displacement conditions applied on  $\widehat{X}^{(3)}$  was the same as the others, while the acted areas were the adhesive circles, as shown in figures. Finally, we also applied rigid rotations with the magnitude of 45 degrees (or more minor if interferences occur) on that areas.

### *Deformation experiment*

All the compression tests were executed by a compressor assembled by Lego Technic parts. The curved surface with positive Gaussian curvature on where DMM-1 and HMM-1 are attached is the wall of a sphere whose diameter is 200mm. The curved surface with negative Gaussian curvature on where DMM-1 is attached is the wall of a bottle whose volume is 5L(Nongfu Spring, P.R.China). The folding of DMM-3 is executed by a frame assembled by Lego Technic parts.

## Data availability

The datasets generated or analyzed during the current study are available from the corresponding author on reasonable request.

## Code availability

The code generated during the current study is available from the corresponding author on reasonable request.

## Competing interests

The authors declare no competing interests.

- 1 Berger, J. B., Wadley, H. N. & McMeeking, R. M. Mechanical metamaterials at the theoretical limit of isotropic elastic stiffness. *Nature* **543**, 533-537, doi:10.1038/nature21075 (2017).
- 2 Xia, X. *et al.* Electrochemically reconfigurable architected materials. *Nature* **573**, 205-213, doi:10.1038/s41586-019-1538-z (2019).
- 3 Jenett, B. *et al.* Discretely assembled mechanical metamaterials. *Sci Adv* **6**, doi:10.1126/sciadv.abc9943 (2020).
- 4 Frenzel, T., Kadic, M. & Wegener, M. Three-dimensional mechanical metamaterials with a twist. *Science* **358**, 1072-1074, doi:10.1126/science.aao4640 (2017).
- 5 Jackson, J. A. *et al.* Field responsive mechanical metamaterials. *Science Advances* **4**, doi:10.1126/sciadv.aau6419 (2018).
- 6 Bertoldi, K., Reis, P. M., Willshaw, S. & Mullin, T. Negative Poisson's ratio behavior induced by an elastic instability. *Adv Mater* **22**, 361-366, doi:10.1002/adma.200901956 (2010).
- 7 Kamrava, S., Ghosh, R., Xiong, J., Felton, S. M. & Vaziri, A. Origami-equivalent compliant mechanism. *Applied Physics Letters* **115**, doi:10.1063/1.5115790 (2019).
- 8 Overvelde, J. T. *et al.* A three-dimensional actuated origami-inspired transformable metamaterial with multiple degrees of freedom. *Nat Commun* **7**, 10929, doi:10.1038/ncomms10929 (2016).
- 9 Melancon, D., Gorissen, B., Garcia-Mora, C. J., Hoberman, C. & Bertoldi, K. Multistable inflatable origami structures at the metre scale. *Nature* **592**, 545-550, doi:10.1038/s41586-021-03407-4 (2021).
- 10 Dieleman, P., Vasmel, N., Waitukaitis, S. & van Hecke, M. Jigsaw puzzle design of pluripotent origami. *Nature Physics* **16**, 63-68, doi:10.1038/s41567-019-0677-3 (2019).
- 11 Liu, B. *et al.* Topological kinematics of origami metamaterials. *Nature Physics* **14**, 811-815, doi:10.1038/s41567-018-0150-8 (2018).
- 12 Choi, G. P. T., Dudte, L. H. & Mahadevan, L. Programming shape using kirigami tessellations. *Nat Mater* **18**, 999-1004, doi:10.1038/s41563-019-0452-y (2019).
- 13 Coulais, C., Kettenis, C. & van Hecke, M. A characteristic length scale causes anomalous size effects and boundary programmability in mechanical metamaterials. *Nature Physics* **14**, 40-44, doi:10.1038/nphys4269 (2017).
- 14 Castle, T. *et al.* Making the cut: lattice kirigami rules. *Phys Rev Lett* **113**, 245502, doi:10.1103/PhysRevLett.113.245502 (2014).
- 15 Cho, Y. *et al.* Engineering the shape and structure of materials by fractal cut. *Proc Natl Acad Sci U S A* **111**, 17390-17395, doi:10.1073/pnas.1417276111 (2014).
- 16 Rafsanjani, A., Jin, L., Deng, B. & Bertoldi, K. Propagation of pop ups in kirigami shells. *Proc Natl Acad Sci U S A* **116**, 8200-8205, doi:10.1073/pnas.1817763116 (2019).
- 17 Chen, T., Pauly, M. & Reis, P. M. A reprogrammable mechanical metamaterial with stable memory. *Nature* **589**, 386-390, doi:10.1038/s41586-020-03123-5 (2021).
- 18 Li, S. *et al.* Liquid-induced topological transformations of cellular microstructures. *Nature* **592**, 386-391, doi:10.1038/s41586-021-03404-7 (2021).
- 19 Overvelde, J. T., Weaver, J. C., Hoberman, C. & Bertoldi, K. Rational design of reconfigurable prismatic architected materials. *Nature* **541**, 347-352, doi:10.1038/nature20824 (2017).
- 20 Haghpanah, B., Salari-Sharif, L., Pourrajab, P., Hopkins, J. & Valdevit, L. Multistable Shape-Reconfigurable Architected Materials. *Adv Mater* **28**, 7915-7920, doi:10.1002/adma.201601650 (2016).
- 21 Coulais, C., Teomy, E., de Reus, K., Shokef, Y. & van Hecke, M. Combinatorial design of textured mechanical metamaterials. *Nature* **535**, 529-532, doi:10.1038/nature18960 (2016).
- 22 Zhang, Y., Li, B., Zheng, Q. S., Genin, G. M. & Chen, C. Q. Programmable and robust static topological solitons in mechanical metamaterials. *Nat Commun* **10**, 5605, doi:10.1038/s41467-019-13546-y (2019).
- 23 Meeussen, A. S., Oğuz, E. C., Shokef, Y. & Hecke, M. v. Topological defects produce exotic mechanics in complex metamaterials. *Nature Physics* **16**, 307-311, doi:10.1038/s41567-019-0763-6 (2020).
- 24 Mitchell, N. P., Nash, L. M., Hexner, D., Turner, A. M. & Irvine, W. T. M. Amorphous topological insulators constructed from random point sets. *Nature Physics* **14**, 380-385, doi:10.1038/s41567-017-0024-5 (2018).
- 25 Paulose, J., Chen, B. G.-g. & Vitelli, V. Topological modes bound to dislocations in mechanical metamaterials. *Nature Physics* **11**, 153-156, doi:10.1038/nphys3185 (2015).

- 26 Nežerka, V. *et al.* A jigsaw puzzle metamaterial concept. *Composite Structures* **202**, 1275-1279, doi:10.1016/j.compstruct.2018.06.015 (2018).
- 27 Widlund, T., Yang, S., Hsu, Y.-Y. & Lu, N. Stretchability and compliance of freestanding serpentine-shaped ribbons. *International Journal of Solids and Structures* **51**, 4026-4037, doi:10.1016/j.ijsolstr.2014.07.025 (2014).
- 28 Yang, S., Qiao, S. & Lu, N. Elasticity Solutions to Nonbuckling Serpentine Ribbons. *Journal of Applied Mechanics* **84**, doi:10.1115/1.4035118 (2017).
- 29 Bertoldi, K., Vitelli, V., Christensen, J. & van Hecke, M. Flexible mechanical metamaterials. *Nature Reviews Materials* **2**, doi:10.1038/natrevmats.2017.66 (2017).
- 30 Kolken, H. M. A. & Zadpoor, A. A. Auxetic mechanical metamaterials. *RSC Advances* **7**, 5111-5129, doi:10.1039/c6ra27333e (2017).
- 31 Yang, W., Liu, Q., Gao, Z., Yue, Z. & Xu, B. Theoretical search for heterogeneously architected 2D structures. *Proc Natl Acad Sci U S A* **115**, E7245-E7254, doi:10.1073/pnas.1806769115 (2018).
- 32 Weiss, T. & Ieee. *Implementing Position-Based Real-Time Simulation of Large Crowds.* (2019).
- 33 Macklin, M. & Mueller, M. Position Based Fluids. *Acm Transactions on Graphics* **32**, doi:10.1145/2461912.2461984 (2013).
- 34 Deul, C., Charrier, P. & Bender, J. Position-based rigid-body dynamics. *Computer Animation and Virtual Worlds* **27**, 103-112, doi:10.1002/cav.1614 (2016).
- 35 Bender, J., Mueller, M., Otaduy, M. A., Teschner, M. & Macklin, M. A Survey on Position-Based Simulation Methods in Computer Graphics. *Computer Graphics Forum* **33**, 228-251, doi:10.1111/cgf.12346 (2014).

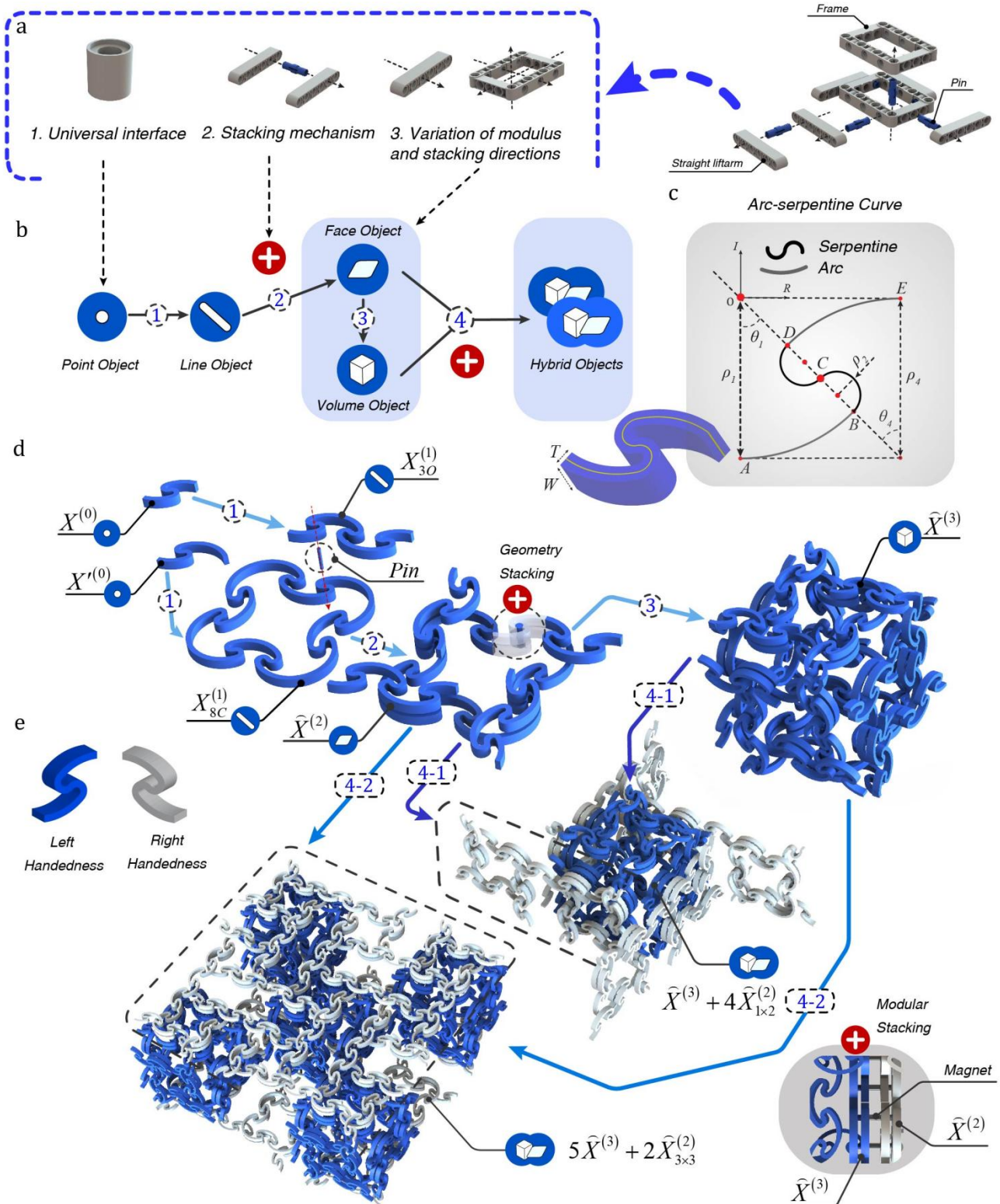


**Figure1. The schematic of the divergent design of the unit-cells.** (a) Three basic elements abstracted from the building mechanism of Lego Technics parts. (b) A deduction process that includes the above basic elements, which transforms the fundamental element (symbolized by a point) into a variety of stackable modules (four of them are shown in the figure and symbolized by face, cube and the hybrids of them, respectively) through a stacking mechanism (symbolized by an adding operator). (c) The geometry of arc-serpentine curve(ASC) and the way materializing it to a point object with width and thickness. (d) The detailed schematic of the deduction process. The standard and varied point objects are deducted(path-1) as two kinds of line objects which are stacked(path-2) with four pins as a face object. This object and its three dimensional derivatives(path-3), including two of their hybrids(path-4-1 and path-4-2), work as the unit-cells of following metamaterials (e) A demonstration of the handedness of point object.

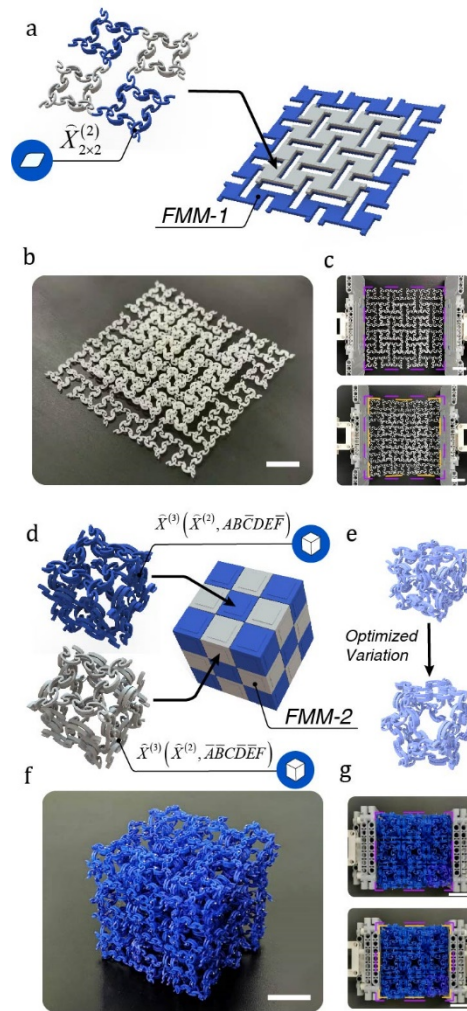


**Figure 2. The building schematic and test of fundamental mechanical metamaterials(FMM).** (a)The schematic of building FMM-1 which are resulted in (b) sheet-like mechanical metamaterials and exhibits (c)auxetic behavior under compression since the boundary of the compressed state(yellow dashed line) is within the one of the initial state(purple dashed line). (d) The schematic of building FMM-2 whose unit-cells are capable of expanding by optimized redesign (e). The corresponding bulk metamaterial(f) exhibits (g)auxetic behavior under compression since the boundary of the compressed state(yellow dashed line) is within the ones of the initial state (purple dashed line). The scale bars in (b-c) are 20mm and in (f-g) are 25mm.

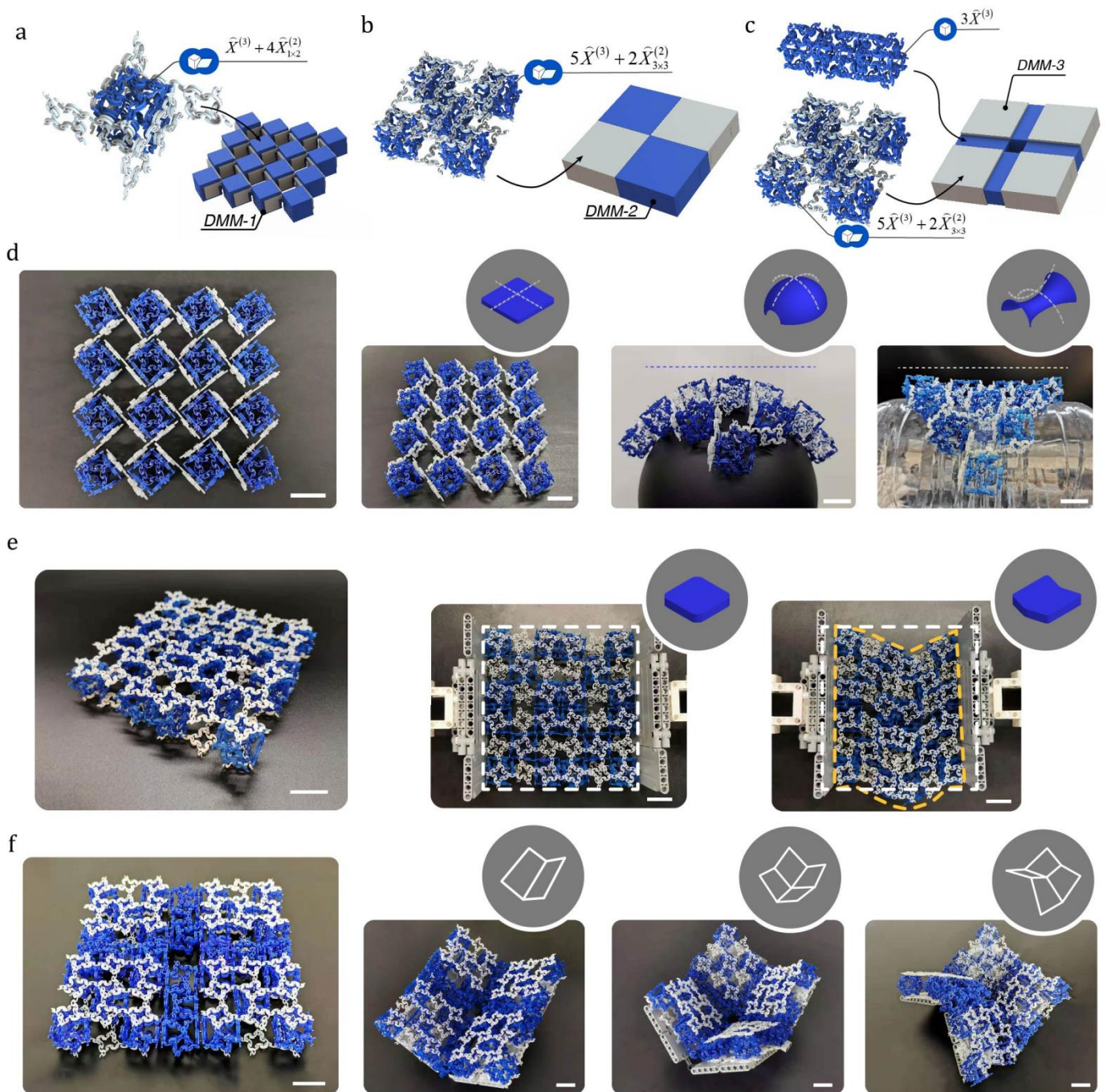


**Figure3. building schematic and demonstration of three types of derivative mechanical metamaterials(DMM).** (a-c) The schematics of building DMM-1, DMM-2, and DMM-3. (d)From left to right: the free-state of DMM-1, the deformation of DMM-1 when it attaches on the surfaces whose Gaussian curvature are zero, positive and negative, respectively. (e)From left to right: the isometric and top view of the free-state of DMM-2, the in-plane deformation of DMM-2 undergoes lateral compression. (f) From left to right: the free-state of DMM-3, the folded deformations of DMM-3 with zero, positive, and negative Gaussian curvature, respectively. The scale bars are 25mm.

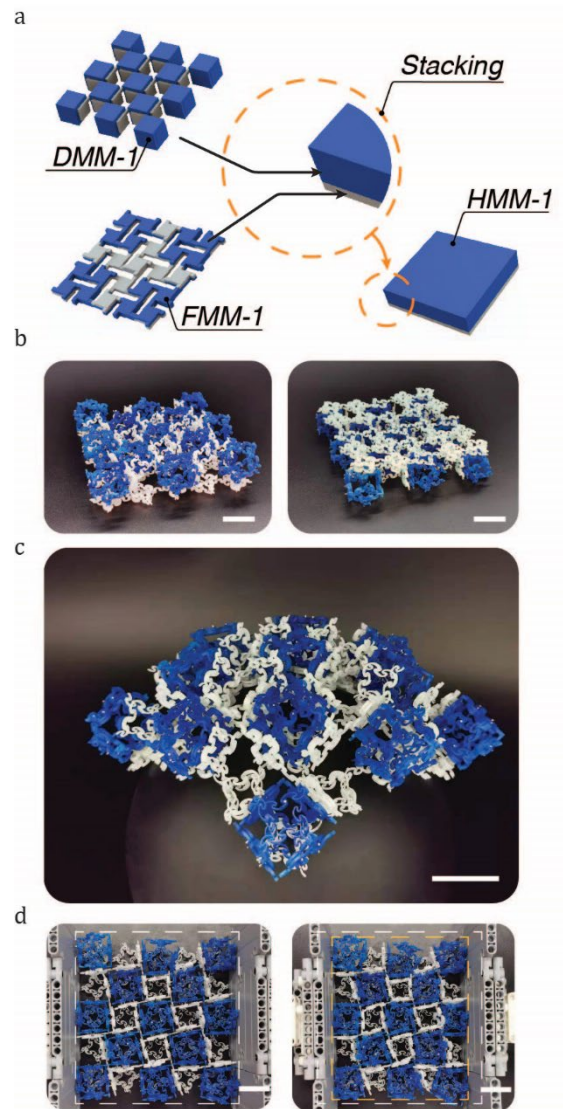
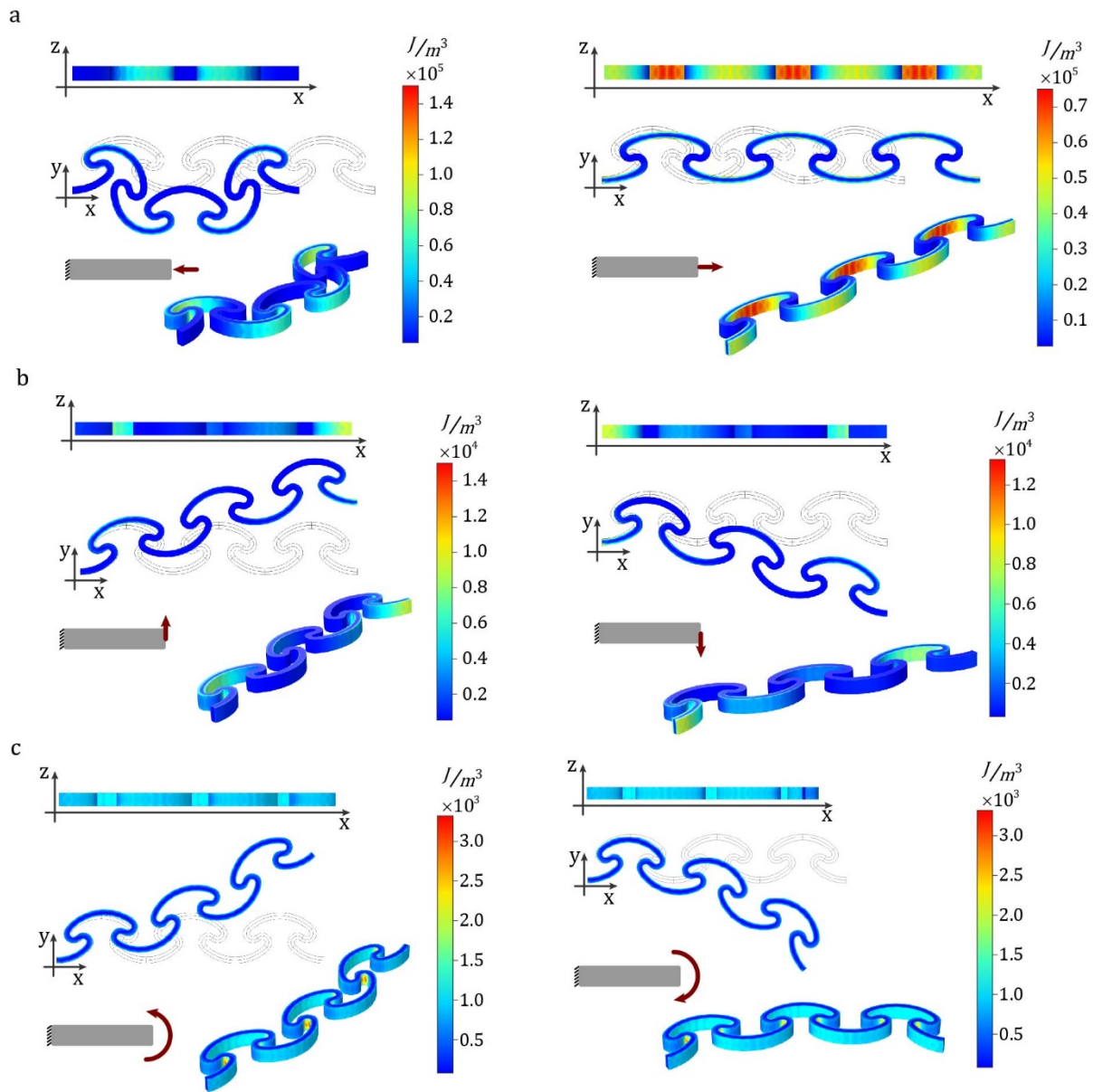
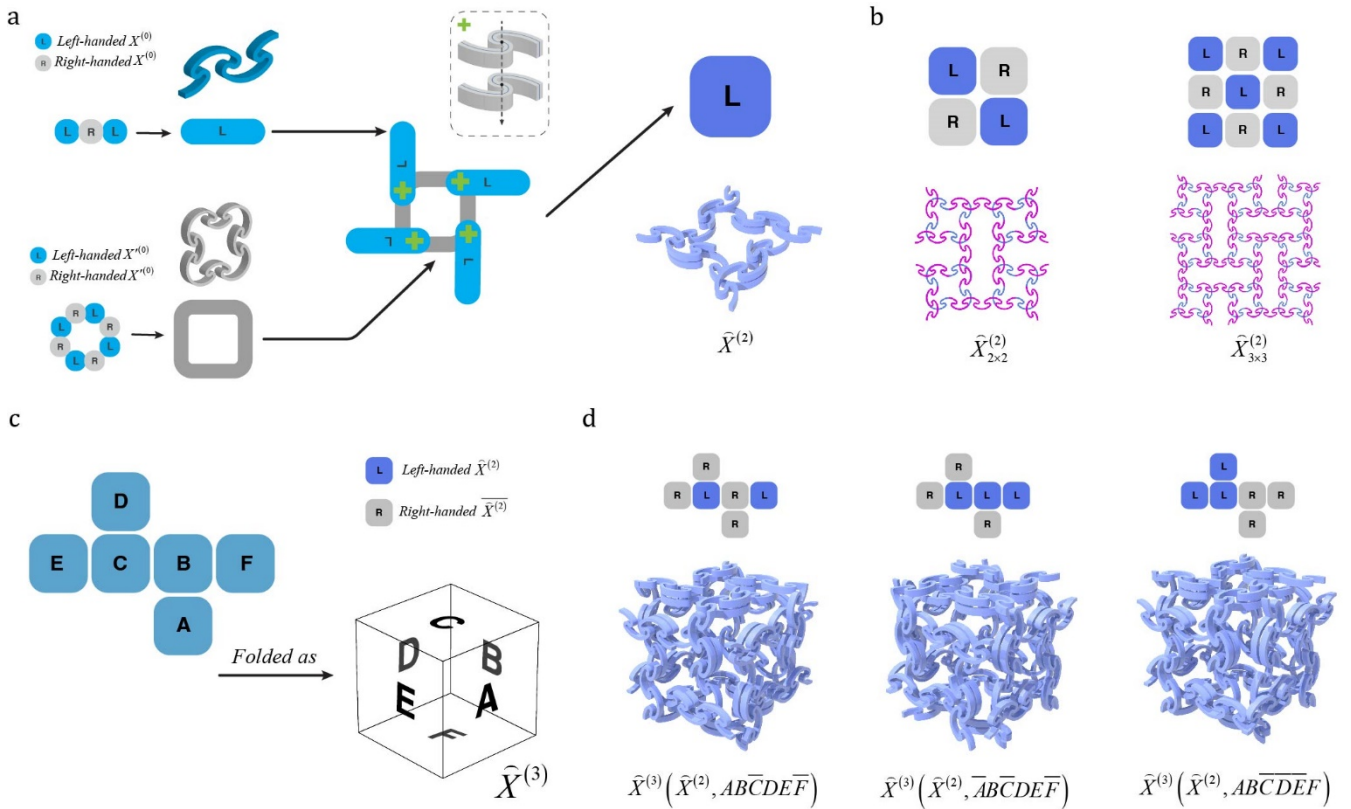


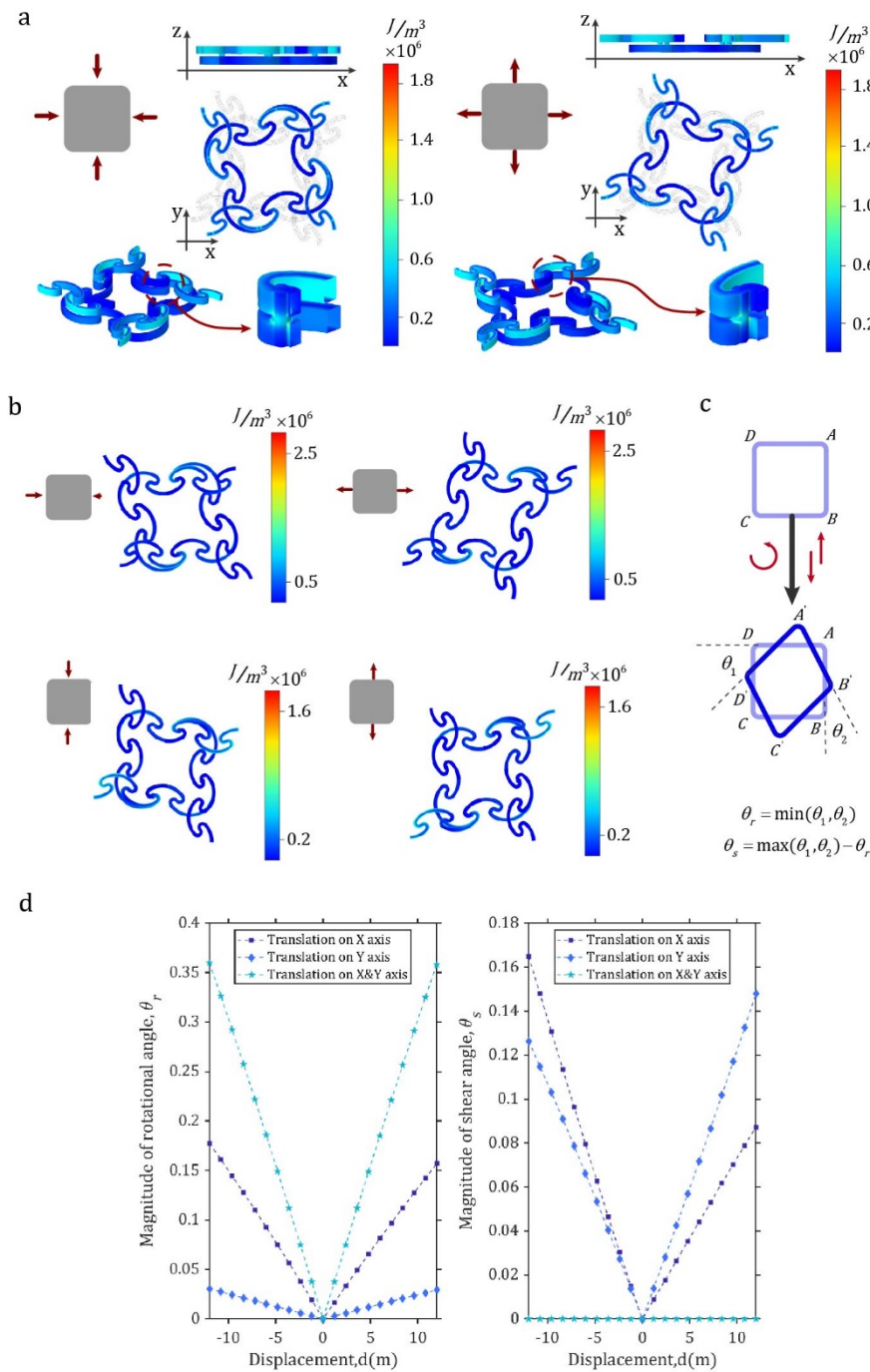
**Figure 4. The building schematic and demonstration of the hybrid mechanical metamaterials (HMM).** (a) The schematic of building HMM. (b) The top and bottom view of HMM. (c) HMM is capable of attaching on a spherical surface compliantly and (d) auxetic undergoing compression. The scale bars are 25mm.



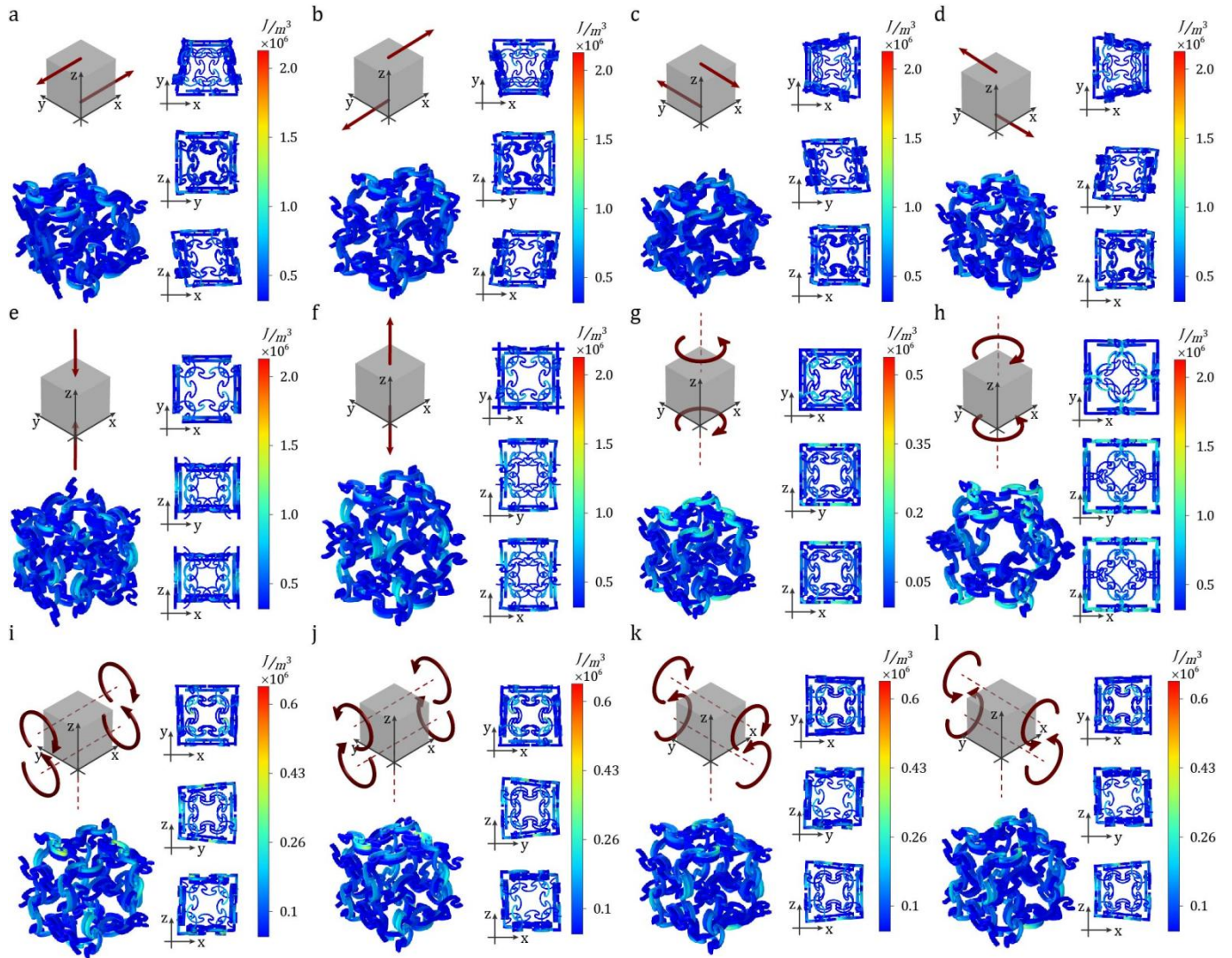
**Extended Data Figure1. The simulation results of the line object consisted of 6 point objects.** (a) From left to right: the deformation of the line object that undergoes compression and stretch, respectively. (b) From left to right: the deformation of the line object that undergoes shearing along the positive and negative direction of the Y-axis, respectively. (c) From left to right: the deformation of the line object that undergoes bending along the positive and negative direction of the Z-axis, respectively. In all six scenes: The colored counter shows the distribution of the elastic energy density caused by deformation. We fixed the left vertex of this line object and applied the above displacements or rotations to the right one. The dashed geometry shows the initial state of the line object.



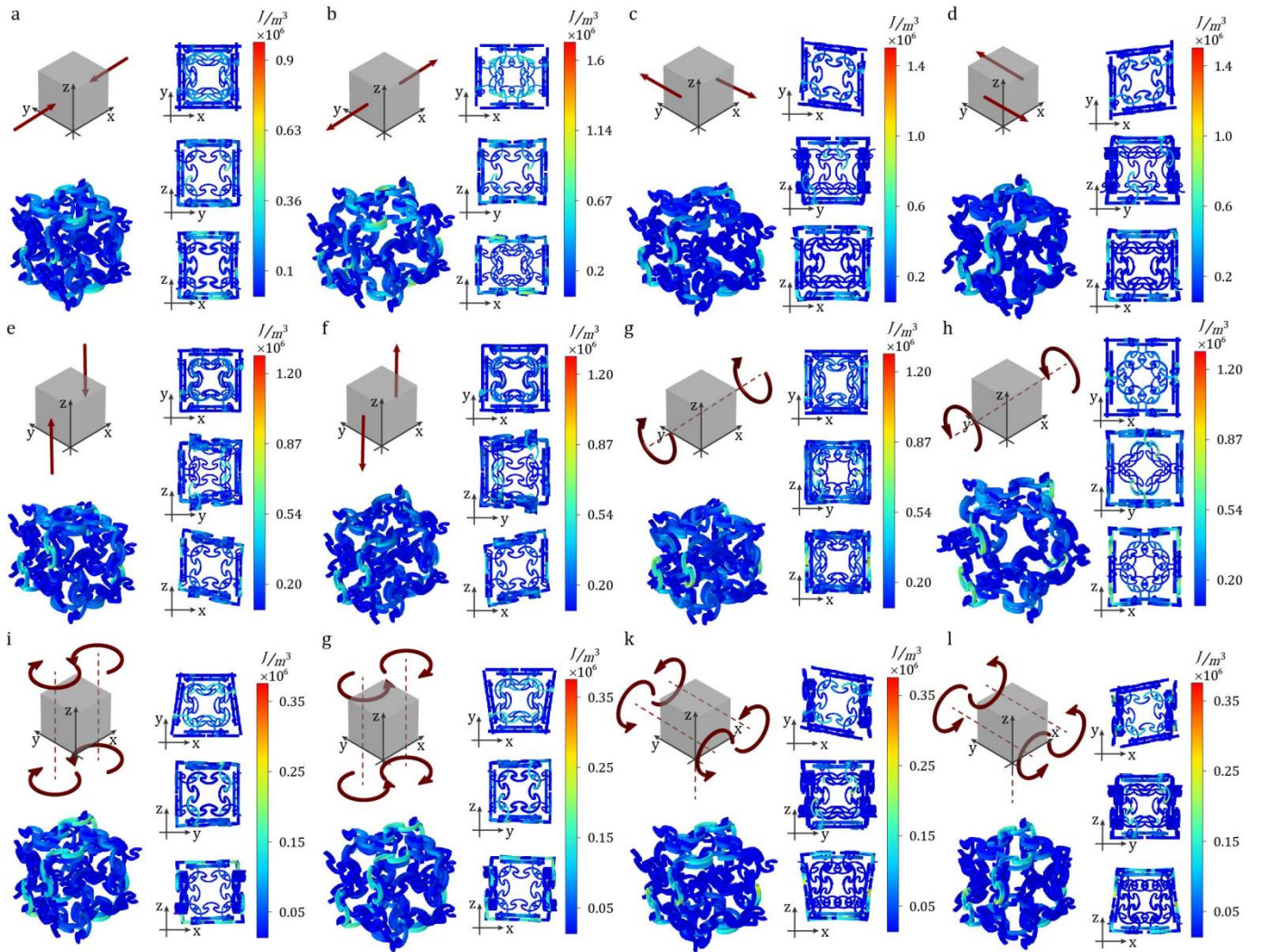
**Extended Data Figure 2. The schematics of building the line, face, and volume object.** (a) The schematics of building open, closed line, and face objects. (b) The demonstration of extended face object. (c) The assignment of each facet of the volume object. (d) Three possible handedness configurations of the volume object.



**Extended Data Figure 3. The simulation results of the face object undergoing two types of boundary conditions.** (a) The top-, front- and perspective view of the deformation of the face object that undergoes compression and stretching along the X- and Y-axis simultaneously. (b) The top-, front- and perspective view of the deformation of the face object that undergoes compression and stretching along the X-axis and Y-axis, respectively. (c) The definition of rotational angle and shear angle of the face object. (d) The angle-displacement data of the face objects undergoing above boundary conditions. In all six scenes: The colored counter shows the distribution of the elastic energy density caused by deformation. We applied prescribed displacements on the four or two vertices of the face object and maintained the rest free.



**Extended Data Figure 4.** The simulation results of the volume object whose acted facets are face-C and face-F. (a-f) The top-, front-, left-, and perspective view of the deformation of the volume object undergoing linear prescribed displacements along the X-, Y-, and Z-axis, respectively. (g-l) The top-, front-, left-, and perspective view of the deformation of the volume object undergoing prescribed rotations along the X-, Y-, and Z-axis, respectively. In all scenes: The colored counter shows the distribution of the elastic energy density caused by deformation. We applied prescribed displacements on face-C and face-F of the volume object and maintained the rest free.



**Extended Data Figure 5. The simulation results of the volume object whose acted facets are face-A and face-D.** (a-f) The top-, front-, left-, and perspective view of the deformation of the volume object undergoing linear prescribed displacements along the X-, Y-, and Z-axis, respectively. (g-l) The top-, front-, left-, and perspective view of the deformation of the volume object undergoing prescribed rotations along the X-, Y-, and Z-axis, respectively. In all scenes: The colored counter shows the distribution of the elastic energy density caused by deformation. We applied prescribed displacements on face-A and face-D of the volume object and maintained the rest free.

Extended Data Table 1 | The list of notations and responsive geometries and unit-cell

Notation	Definition	Stacking type	Thumbnail	
ASC	Arc-serpentine curve	None		
$X^{(0)}$	Point object with left-handedness	None		
$\overline{X^{(0)}}$	Point object with right-handedness	None		
$X^{(0)}$	Left-handed point object with varied parameter	None		
$X^{(1)}$	$X_{nO}^{(1)}$	Open line object consisted of n point objects		
	$X_{nC}^{(1)}$	Closed line objects consisted of n point objects		
$X^{(2)}(X_{nO}^{(1)}, p, X_{mC}^{(1)}, q)$	Face object consisted of p $X_{nO}^{(1)}$ s and q $X_{mC}^{(1)}$ s	Magnetic		
$\overline{X^{(2)}} = X^{(2)}(X_{3O}^{(1)}, 4, X_{8C}^{(1)}, 1)$	Left-handed specific face object consisted of four $X_{3O}^{(1)}$ s and one $X_{8C}^{(1)}$	Magnetic		
$\overline{X^{(2)}}$	Right-handed specific face object consisted of four $X_{3O}^{(1)}$ s and one $X_{8C}^{(1)}$	Magnetic		
$\overline{X_{3 \times 3}^{(2)}}$	Extend face object consisted of a 3x3 pattern whose element is $\overline{X^{(2)}}$	Magnetic		
$X^{(3)}(X^{(2)}, \Xi)$	Volume object consisted of $X^{(2)}$ with a handedness configuration $\Xi$	Magnetic		
$\overline{X^{(3)}} = X^{(3)}(\overline{X^{(2)}}, ABCDEF)$	Specific volume object consisted of $\overline{X^{(2)}}$ with a given handedness configuration $ABCDEF$	Magnetic		
$X^{(4)}$	$X^{(4)}(\overline{X^{(3)}} + 4\overline{X_{3 \times 2}^{(2)}})$	Blend object consisted of one $\overline{X^{(3)}}$ and four $\overline{X_{3 \times 2}^{(2)}}$ s	Magnetic	
	$X^{(4)}(5\overline{X^{(3)}} + 2\overline{X_{3 \times 3}^{(2)}})$	Blend object consisted of five $\overline{X^{(3)}}$ s and two $\overline{X_{3 \times 3}^{(2)}}$ s	Magnetic	

## Supplementary Files

This is a list of supplementary files associated with this preprint. Click to download.

- [SupplementaryInformation.docx](#)